This document is the Accepted Manuscript version of a Published Work that appeared in final form in Environmental science and technology, copyright © 2020 American Chemical Society after peer review and technical editing by the publisher. To access the final edited and published work see https://doi.org/10.1021/acs.est.0c05235.

The following publication He, C., Wang, Y., Li, Z., Huang, Y., Liao, Y., Xia, D., & Lee, S. (2020). Facet engineered α-MnO2 for efficient catalytic ozonation of odor CH3SH: oxygen vacancy-induced active centers and catalytic mechanism. Environmental science & technology, 54(19), 12771-12783.

Engineering Crystal Facet of α-MnO2 for Efficient Catalytic Ozonation of Odor CH3SH: Oxygen Vacancy-Induced Active Centers and Catalytic Mechanism

Journal:	*Environmental Science & Technology*
Manuscript ID	es-2020-040764.R1
Manuscript Type:	Article
Date Submitted by the Author:	n/a
Complete List of Authors:	He, Chun; Sun Yat-sen University, China, Environmental Science and Engineering Wang, Yunchen; Sun Yat-Sen University Li, Zhiyao; Sun Yat-Sen University Liao, Yuhong; Sun Yat-Sen University Xia, Dehua; Sun Yat-sen University, School of Environmental Science and Engineering Lee, Shun Cheng; The HongKong Polytechnic University, Department of Civil and Structural Engineering

Engineering Crystal Facet of α-MnO_2 for Efficient Catalytic Ozonation of Odor CH_3SH: Oxygen Vacancy-Induced Active Centers and Catalytic Mechanism

Chun He [a, b], Yunchen Wang [a], Zhiyao Li[a], Yuhong Liao[a], Dehua Xia [a, b, *], Shuncheng Lee[c]

[a] *School of Environmental Science and Engineering, Sun Yat-sen University, Guangzhou, 510275, CHINA*

[b] *Guangdong Provincial Key Laboratory of Environmental Pollution Control and Remediation Technology, Guangzhou, 510275, CHINA*

[c] *Department of Civil and Structural Engineering, Hong Kong Polytechnic University, Hong Kong, China*

[*] Corresponding author: School of Environmental Science and Engineering, Sun Yat-sen University, Guangzhou, 510275, China. Tel.: +86 20 39332690. Email address: xiadehua3@mail.sysu.edu.cn (D.H. Xia).

Abstract

The oxygen vacancy in MnO_2 is normally considered as the active site for catalytic ozonation, and acquiring a highly reactive crystal facet with abundant oxygen vacancy by facet engineering is highly desirable for improving the catalytic reactivity. Herein, three facet-engineered α-MnO_2 was prepared and successfully utilized for catalytic ozonation towards an odorous CH_3SH. The as-synthesized 310-MnO_2 exhibited superior activity in catalytic ozonation of CH_3SH than that of 110-MnO_2 and 100-MnO_2, which could achieve 100% removal efficiency for 70 ppm of CH_3SH within 20 min. The results of XPS, Raman, H_2-TPR, and DFT calculation all confirm that the (310) facets with higher surface energy than other facets can feature the formation of oxygen vacancies, which facilitate the adsorption and activate O_3 into intermediate peroxide species (O^{2-}/O_2^{2-}) and reactive oxygen species ($\bullet O_2^-/^1O_2$) for eliminating adjacent CH_3SH. *In-situ* diffuse reflectance infrared Fourier transform spectroscopy (*In-situ* DRIFTS) revealed that the CH_3SH was chemisorbed at S atom to form CH_3S^-, which was further converted into intermediate $CH_3SO_3^-$ and finally oxidized into SO_4^{2-} and CO_3^{2-}/CO_2 during process. Attributed to the deep oxidation of CH_3SH on 310-MnO_2 via efficient cycling of active oxygen vacancies, the lifetime of 310-MnO_2 can be extended to 2.5 h with limited loss of activity, while 110-MnO_2 and 100-MnO_2 were inactivated within 1 h. This study deepens the comprehension of facet-engineering in MnO_2 and presents an efficient and portable catalyst to control odorous pollution.

Keywords: Crystal facet engineering, α-MnO_2, CH_3SH, catalytic ozonation, density functional theory

1. Introduction

Methyl mercaptan (CH_3SH), a typical sulfur containing odorous gas (S-VOCs) with high toxicity and corrosiveness, widely released from sewage treatment and sanitary landfill.[1-3] The exposure of CH_3SH at few ppm-level can give human an unpleasant feeling and dozens of ppm-level can cause significant poisoning[2-3]. To date, considerable efforts have been devoted to control CH_3SH, including adsorption, biological treatment, incineration, plasma technology and catalytic conversion.[3-7] Catalytic combustion with high efficiency is the most promising technology, because S-VOCs are converted to CO_2 and H_2O or less toxic products. However, the catalytic temperature is generally higher than 200 °C, which increases the energy consumption and the catalysts are prone to sintering. Therefore, the catalytic combustion may not be cost-effective for CH_3SH removal from industrial activities with the concentrations ranging from few to hundreds of ppm. Currently, catalytic ozonation has attracted much attention because of its capacity to oxidize CH_3SH at various concentrations under mild conditions.[8, 9] Especially, due to the nonselective oxidation and efficient mineralization of VOCs, catalytic ozonation causes no great accumulation of intermediates and limited deactivation of catalysts.[10] Moreover, as an electrophilic molecule, O_3 prefers to react with high electronic density sites of molecules such as CH_3SH having carbon-carbon or carbon-sulfur bonds.

In most studies, noble metals, transition metals, and their derived mixed oxides (especially MnO_2), are commonly used in the catalytic ozonation, depending on its plentiful valence states, versatile structures, high stability and low cost. Till now, different crystal structures like α-, β-, γ- and δ-MnO_2, and different morphologies like rod-, wire-, tube- and flower-like MnO_2 are designed to achieve efficient catalytic ozonation. However, limited studies devoted to the dependence of reactivity on crystal facets of MnO_2[1,11-13]. Generally, crystal facet engineering can induce specific physicochemical properties in catalysts, owing to the distorted electronic structure and different exposed atoms in the surface of different facet engineered catalysts.[14-16] For instance, by tuning the morphology and ratio of different facets such as (100), (110), (310), the catalytic reactivity of MnO_2 for HCHO decomposition could be evidently boosted due to the enhanced adsorption/activation of O_2 and H_2O by higher oxygen vacancy on (310) facet.[17-19] Aside from the facet reforming and growth, a large amplitude of catalytically active regions is indispensable for exposed surface-active complexes within facet-dominated surfaces. Motivated by this work, the identified property of facet engineered MnO_2 infers its great potential for catalytic ozonation of CH_3SH.

In general, the catalytic ozonation pathway proceeds by the adsorption and decomposition of O_3 to atomic oxygen species and derived reactive oxygen species (ROS) on the catalyst, both steps have an imperative bearing on the efficiency of catalytic ozonation.[14-16] As identified, the affinity and reactivity with reactants and pollutants are both tightly related to the kind of crystal facets, and a high-index facet with high percentage of under-coordinated atoms and defects (especially oxygen vacancy) always exhibit high surface energy to capture neighbouring molecular.[17] Oyama and his coworkers have proposed that oxygen vacancy of MnO_2 was likely the active center for ozone adsorption and decomposition.[20] Therefore, the high energy facet of MnO_2 with higher oxygen vacancy is expected to achieve enhanced catalytic ozonation. On the other hand, competitive adsorption between O_3 and pollutants always happen during catalytic ozonation, which is the critical step for the whole catalytic process. Therefore, the adsorption and catalytic ability of O_3 towards CH_3SH by facet engineered MnO_2 need require further research.

α-MnO_2 has been proved for a superior performance in catalytic decomposition toward O_3 than β-, γ- and δ-MnO_2, as the tunnel structure of α-MnO_2 exposed more MnO_6 edges for ozone adsorption and interface reaction.[1,13,21,22] Hence, α-MnO_2 with exposed three major (100), (110) and (310) facet-dominated surfaces were systematically studied for catalytic ozonation of S-VOCs in terms of activity and selectivity, formation of oxygen vacancies, identification of catalytic active sites, and intermediate pathways. The density functional theory (DFT) calculations were also used to investigate the difference in the adsorption and catalytic activity of facet α-MnO_2 towards O_3. Moreover, the efficient 310-MnO_2 catalysts were immobilized on the mesoporous Al_2O_3 as substrates to evaluate their removal effectiveness. The present work offers a promising way to tune the crystal facets of metal oxides and model it into a portable shape for practical environmental remediation.

2. Experimental Section

2.1 Sample Preparation

(1) 310-α-MnO_2: 20.0 mmol of $KMnO_4$ and 10.0 mmol of $(NH_4)_2C_2O_4 \cdot H_2O$ were dissolved in 70 mL of deionized water under vigorous magnetic stirring. The mixture was then transferred to a 100 mL stainless-steel autoclave and kept at 180 °C for 24 h. The resulting precipitates were collected via centrifugation, washed and dried. To prepare α-MnO_2-310/Al_2O_3 (310-Mn/Al): 3 g of γ-Al_2O_3 was impregnated into the solution of $KMnO_4$ and $(NH_4)_2C_2O_4 \cdot H_2O$ followed by an ultrasonic bath for 3 h and then magnetically stirred for 24 h to assure a sufficient absorption. Other processes are same with 310-α-MnO_2. (2) 110-α-MnO_2: it was prepared by the same method with 310-α-MnO_2, but the reactant of $(NH_4)_2C_2O_4$ was replaced by $(NH_4)_2SO_4$. (3) 100-α-MnO_2: 8.0 mmol of $MnSO_4 \cdot H_2O$, 8.0 mmol of $(NH_4)_2S_2O_8$, 15.0 mmol of $(NH_4)_2SO_4$, and 8.0 mmol of KNO_3 were dissolved in 40 mL of deionized water under vigorous magnetic stirring to form a precursor solution. The mixture was then transferred to a 100 mL autoclave and kept at 120 °C for 20 h. The resulting precipitates were collected via centrifugation, washed and dried.

2.2 Sample Characterization

X-ray diffraction (XRD) analysis of the samples was performed on a Rigaku D/MAX 2500 X-ray diffractometer equipped with a Cu Kα radiation source. The morphology of the samples was examined by scanning electron microscopy (SEM, 5 kV) and transmission electron microscopy (TEM, 300 kV, JEM-2010HR) at 5 kV, respectively. Nitrogen adsorption-desorption isotherms of the samples were obtained at 77 K on a Gemini VII 2390 surface area analyzer (MQL). The chemical compositions of the catalysts were determined by X-ray photoelectron spectroscopy (XPS, ESCALAB 250, Thermo Fisher Scientific, USA). Hydrogen temperature-programmed reduction (H_2-TPR) analysis was performed on the 80 BELCAT-B (Japan) instrument. Raman spectra was obtained using a Laser Micro-Raman Spectrometer (Renishaw inVia, British) with a 514.5 nm laser source. *In-situ* DRIFTS was recorded on Thermo Fisher 6700. The CV curves were obtained on a CHI 660E electrochemical workstation equipped with a standard three-electrode system (a platinum foil as the counter electrode and saturated calomel electrode (SCE) as a reference electrode) using 0.5 M Na_2SO_4 buffer.

2.3 CH_3SH Removal Test

The elimination of CH_3SH with catalytic ozonation was carried out using a continuous flow reactor as shown in Figure S1. The fixed bed quartz tube reactor (Φ1.5 cm) was padded with 0.1 g of facet engineered MnO_2 powder. For each test, the CH_3SH and N_2 were premixed in a container to adjust the initial concentration of CH_3SH maintained at 70 ppm with a flow rate of 0.18 L/min. O_3 was produced by an ozone generator (YDG, YE-TG-02PH) with an initial concentration at 2.0 mg/L and a flow rate of 0.02 L/min. The inlet and outlet concentrations of CH_3SH were continuously monitored by a CH_3SH sensor (Detcon, DM-400IS). The total gas stream velocity was kept at 0.2 L/min.

2.4 Reactive species tests

In radicals inhibiting tests, tert-butanol (TBA) was used as hydroxyl radical (•OH) scavenger; ascorbic acid was used to suppress superoxide radical ($•O_2^-$) and NaN_3 was used to trap singlet oxygen ($^1O_2$), respectively.[23, 24] The catalysts were immersed into 25.0 mM of above trapping agents and ultrasonicated for 15 min, followed by filtration and dried, then applied for catalytic ozonation of CH_3SH. For electron spin resonance (ESR) detection of radicals, 5, 5-dimethyl-1-pyrrolineN-oxide (DMPO) was used to trap •OH and $•O_2^-$, then 2,2,6,6-Tetramethylpiperidine (TEMP) was used to trap $^1O_2$. In detail, the samples for ESR tests were dispersed in a 100 mM DMPO/TMPO solution (2 mL) with O_3 purging, and the solvent was H_2O for trapping •OH and $^1O_2$, methanol for trapping $•O_2^-$.[25, 26]

2.5 DFT Calculation Method

The different exposed facets of MnO_2 were studied by first-principles calculations density-functional theory (DFT) as implemented in the VASP code with projector-augmented wave (PAW) pseudopotentials.[27, 28] The electronic structure was calculated using the Generalized Gradient Approximation (GGA) of Perdew-Burke-Ernzerhof with Hubbard U corrections (PBE+U).[29-31] To obtain the equilibrium lattice parameters by relaxation of the bulk cell, a cutoff for the plane wave basis set of 520 eV was used to avoid Pulay stress. Geometry structures were fully relaxed until the convergence criteria of energy and force are less than 10^{-8} eV and 0.05 eV/Å, respectively. The lattice constants of α-MnO_2 was set as $a = b = 9.75$ Å, $c = 2.86$ Å. The calculations afterwards were performed based on the obtained equilibrium lattice constants using a cutoff energy of 400 eV, and a minimum of 3×3×9 k-points was used for each calculation. The surface energy of different facets was also computed, and the specific method was defined as follows (Equation 1):

$$\gamma = \frac{E_s - nE_b}{2A} \qquad \text{Eq. 1}$$

where E_s is the energy of a slab containing n formula units and E_b is the total energy per formula unit. A is the area of the slab surface, and the factor of 2 represents that there are two surfaces for each slab.

3 Results and discussion

3.1 Catalyst Structure and Morphology

X-ray diffraction (XRD) was firstly used to determine the crystalline structure and purity of three facet-engineered MnO_2.[32-34] As shown in Figure 1a, all the pure MnO_2 samples exhibit distinct peaks at 12.8°, 18.1°, 28.9°, 37.6°, 49.9° and 60.2°, corresponding to the diffraction plane of (110), (200), (310), (211), (411) and (521), respectively, well indexed to the tetragonal α-MnO_2 phase (JCPDS, PDF #44-0141). Through comparing the intensities of peaks in (310), (110) and (100) (Figure 1b), an obvious distinction can be observed in the relative ratio of their strength: for 310-MnO_2, the diffraction peak referring to (310) is clearly more intense and sharper with respect to the peaks in (110) and (100). The ratio of (310): (110): (100) in the zoomed XRD pattern of 310-MnO_2 is 2.27:1.12:1 (Figure 1b). As for 110-MnO_2, the (110) peak is the strongest among the three facet MnO_2; similarly, the intensity of major (100) facet obviously ascends in 100-MnO_2, and these characteristics are in well accordance with a former research.[35] These results verify the successful preparation of MnO_2 with different exposed facet.

Raman spectroscopy was recorded to show the bulk structure of as-prepared catalysts.[36-37] As can be seen in Figure 1c, the peaks at around 625 cm^{-1} attributes to the symmetric stretching vibrations v_2(Mn-O) perpendicular to the direction of the [MnO_6] groups,[38] and the band at about 580 cm^{-1} can be assigned to the stretching vibration v_3(Mn-O) in the basal plane of [MnO_6] chains.[39] The calculated ratios of peak intensity between v_2(Mn-O) and v_3(Mn-O) peaks follow the order: 110-MnO_2 (1.046) >100-MnO_2 (0.998) > 310-MnO_2 (0.963) (Table S1), indicating that 310-MnO_2 possesses the most abundant surface defects,[40] which are beneficial to form oxygen vacancies. Moreover, according to the Hooke's law,[41] an equation can be applied to calculate the Mn-O bond force constant (k) as follow, which represents the Mn-O bond strength (Eq. 2).

$$\omega = \frac{1}{2\pi c}\sqrt{\frac{k}{\mu}} \qquad \text{Eq. 2}$$

where ω is the Raman shift (cm^{-1}), c is light velocity, and μ is effective mass.

Obviously, all the peaks of 310-MnO_2 exhibit the lowest Raman shift (ω) among the three MnO_2, indicating that 310-MnO_2 owns the lowest k constant on the basis of the equality of relevant parameters other than ω. The results confirm that the highly active facets of 310-MnO_2 could lead to the weakening of Mn-O bonds. This means the decrease of oxygen escaping energy is conducive to the formation of oxygen vacancies and thus facilitates the mobility of oxygen species. Moreover, it is generally accepted that a facet with a high percentage of unsaturated atoms always possesses a superior reactivity to that with a low percentage of unsaturated atoms.[42, 43] Therefore, these high-index facets in the 310-MnO_2 could possess a high density of under-coordinated atoms, such as steps, edges, and kinks, and serve as active sites for catalytic ozonation.[44]

The morphologies and microstructures of the facet engineered MnO_2 catalysts were further investigated by SEM and TEM analysis. As shown in Figure 1d1-f3, all the facet engineered MnO_2 are formed as clusters of nanowires. Under higher magnification, it can be seen that both 110-MnO_2 and 100-MnO_2 nanowires exhibit similar diameter of 70~80 nm, while 310-MnO_2 nanowires show a smaller diameter of around 50 nm. HRTEM images further demonstrate the exposed crystalline facets of different facet engineered MnO_2 (Figure 1d4-f4), the lattice spacings of 0.31, 0.69 and 0.49 nm are consistent well with the values of 3.09, 6.92 and 4.90 Å for the (310), (110) and (100) planes of a-MnO_2 (JCPDS, PDF #44-0141), respectively. Especially, in view of α-MnO_2 usually grows along (001) direction (c axis), and four side walls will be the major exposed facets, it can be found that the 310-MnO_2 owns four (310) facets exposed on the side walls.[32] Consistently, similar phenomenon was also found in 110-MnO_2 and 100-MnO_2.

3.2 Characteristics of Oxygen Vacancies

Generally, the surface element composition and element oxidation state play a decisive role in the catalytic ozonation. XPS was conducted to characterize the surface element composition and chemical states of the as-prepared facet MnO_2. As shown in Figure 2a, the Mn-2p3/2 spectra can be deconvoluted into three peaks with binding energy at 640.6 eV, 641.6 eV and 642.9 eV, corresponding to Mn^{2+}, Mn^{3+}, and Mn^{4+}, respectively.[13] The molar ratio of Mn^{2+}+Mn^{3+}/Mn^{4+} was quantified and summarized in Table S2, following the order of 310-MnO_2 (1.15) > 110-MnO_2 (0.95) > 100-MnO_2 (0.94). Meanwhile, the average oxidation state (AOS) of Mn was calculated by the formula: $AOS = 8.956 - 1.126\Delta Es$ (ΔEs represents the difference in the binding energy between the two Mn-3s peaks). The lowest AOS of 310-MnO_2 (3.394) also suggests that the 310-MnO_2 contains a higher content of low valence Mn than other facet MnO_2 (Figure 2b).[11] It is commonly recognized that low valent Mn could result in the Jahn-Teller distortion and thus facilitate oxygen vacancy formation to maintain charge conservation based on the following process (Eq. 3),[11,13,44] and oxygen vacancies always work as active sites in the catalytic ozonation.[13] Therefore, it is reasonable to deduce that higher oxygen vacancy density are survived in 310-MnO_2, which could be beneficial for catalytic ozonation than other facet MnO_2.

$$4Mn^{4+} + O^{2-} \rightarrow 4Mn^{4+} + 2e^{-}/V_O + 1/2\ O_2 \rightarrow 2Mn^{4+} + 2Mn^{3+} + V_O + 1/2\ O_2 \quad \text{Eq. 3}$$

Moreover, the O 1s spectra (Figure 2c) can be divided into three peaks at 529.7-530.3 eV, 531.4-531.8 eV and 532.9-533.7 eV, corresponding to the lattice oxygen (O_{latt}), low-coordinated oxygen species adsorbed in oxygen vacancies (O_{ads}, such as O^{2-}, O^{-}, and OH group), and hydroxyl species of surface-adsorbed water molecules (O_{surf}), respectively.[34, 35] Generally, the amount of O_{ads} represents the surface oxygen vacancy concentration in catalysts, because oxygen molecules are usually adsorbed at oxygen vacancies and evolved into O_{ads} on catalysts' surface.[13] Therefore, the molar ratio of O_{ads}/O_{latt} descends in the sequence of 310-MnO_2 (0.41) > 110-MnO_2 (0.26) > 100-MnO_2

(0.25), suggesting that 310-MnO_2 is beneficial for the formation of surface oxygen vacancies. Consistently, the Mn/O ratios of 310-MnO_2, 110-MnO_2 and 100-MnO_2 are estimated to be 0.53, 0.53 and 0.51 (Table S2), mainly due to the more oxygen vacancies formed in 310-MnO_2, accordant well with Raman results.[36, 37]

The O_2-TPD spectra is also analyzed to understand the roles of oxygen species within the different exposed facets, which is related to the formation of oxygen vacancies. As shown in Figure 2g, the chemisorbed oxygen species and active surface oxygen usually desorb at lower temperatures around 350 °C, and the higher temperature desorption peak (500-650 °C) is ascribed to the subsurface lattice oxygen from MnO_2 into Mn_2O_3/Mn_3O_4. The higher temperature peak at 700 °C is attributed to the conversion of bulk lattice oxygen. The lower the temperature at which oxygen is released, the looser it is bound to Mn atoms within the framework. Therefore, the 310-MnO_2 has a higher oxygen mobility. Especially, the total peak area for 310-MnO_2 is obviously larger than the other catalysts, indicating that the former has more excellent oxygen adsorption and storage capacity, which corresponded to the higher formation of oxygen vacancies in the 310-MnO_2 and consistent with the O 1s XPS spectra.

EPR measurement was further performed to confirm the oxygen vacancy concentration in three MnO_2 catalysts (Figure 2h). The signal located at around g = 2.003 is ascribed to oxygen vacancies. Generally, the higher the peak intensity, the higher the oxygen vacancy concentration. The sequence of peak intensity is 310 > 110 > 100, further indicating that the 310-MnO_2 catalyst has higher oxygen vacancies than the other two catalysts.

3.3 Reducibility of Catalysts

Since a higher reduction ability was beneficial for catalysts to yield a higher catalytic ozonation, H_2-TPR measurements were thus carried out to further evaluate the reducibility of as-prepared MnO_2. As depicts in Figure 3a, both 110-MnO_2 and 100-MnO_2 contain two peaks of H_2 consumption, assigned to the continuous reduction process of $MnO_2 \rightarrow Mn_2O_3 \rightarrow MnO$, respectively.[12] In contrast, the 310-MnO_2 exhibits only one overlapped reduction peak at 354 ℃, mainly caused by the over-close distance between two peaks. Especially, the 310-MnO_2 shows the lowest temperature of reduction peak among the three catalysts, indicating it owns the highest mobile oxygen species. Coincidently, the onset reduction temperature for all the facet-engineered MnO_2 also follows the order of 310-MnO_2 < 110-MnO_2 < 100-MnO_2 (the inset of Figure 3a). Moreover, 310-MnO_2 has the lowest H_2 consumption during the whole treatment, which is related to the formation of the maximum oxygen vacancies within 310-MnO_2 obtained in O_2-TPD profiles (Figure 2g). The easy reducibility of 310-MnO_2 may be due to the formation of more abundant oxygen vacancies on its surface, which greatly boosts the mobility of oxygen species and facilitates the formation of active oxygen for catalytic ozonation.

Moreover, the CV (cyclic voltammetry) curves were conducted to directly identify the redox reactivity of different facet-engineered MnO_2. As shown in Figure 3b, the anodic current oxidation peaks are corresponded to the oxidation process from $Mn^{2+} \rightarrow Mn^{3+}$ to $Mn^{3+} \rightarrow Mn^{4+}$, conversely, the cathodic current reduction peaks are related to the reduction process from $Mn^{4+} \rightarrow Mn^{3+}$ to $Mn^{3+} \rightarrow Mn^{2+}$. Obviously, the current intensity of both reduction and oxidation curves for 310-MnO_2 are significantly higher than the other two catalysts, illustrating the higher surface charges in Mn species of 310-MnO_2.[46] Therefore, it can be proposed that the 310-MnO_2 owns the best ability to perform a redox cycle, which is vital for continuous catalytic ozonation.[47] What's more, with O_3 purging, the curve of 310-MnO_2 turns to be broader, indicating that O_3 could give impetus to the redox process.

3.5 Catalytic Performance for CH_3SH decomposition

3.5.1 Adsorption and Catalytic Ozonation of CH_3SH by Facet engineered MnO_2

Accordingly, the adsorption ability of 310-MnO_2 for CH_3SH was firstly explored (Figure 4a). In the presence of 310-MnO_2 alone, the reaction reached adsorption equilibrium within 200 s and maintained at 44.2% removal of CH_3SH within 600 s, higher than that of 110-MnO_2 (37.9%) and 100-MnO_2 (30.9%). These results confirm that 310-MnO_2 are optimum for CH_3SH adsorption. After the adsorption equilibrium was attained, then the performance of catalytic ozonation using different catalysts was investigated. As plotted in Figure 4b, facet engineered MnO_2 exhibits obvious facet dependent catalytic performance, i.e. the activities followed the order of 310-MnO_2 > 110-MnO_2 > 100-MnO_2. With respect to 310-MnO_2, in initial 300 s period, the catalytic degradation efficiency increased significantly, whereas the catalytic degradation trend for the 310-MnO_2 reached a relatively stable trend during 400-900 s period. This is because the concentration of CH_3SH in the rection system decreases rapidly due to the catalytic degradation of 310-MnO_2, then quickly decreased to their minimum values along with time extension. Within 1200 s reaction, 310-MnO_2 can realize 100% removal efficiency for 70 ppm of CH_3SH, significantly higher than that of 110-MnO_2 (82.9 %) and 100-MnO_2 (71.5 %), verifying the high percentage of high index facet (310) can readily facilitate the catalytic ozonation. To illustrate deeply, the rate constants for the catalytic ozonation (k) were calculated based on the pseudo first-order kinetics for the initial 300 s reaction (Eq. 4).

$$\text{In}\frac{C}{C_0} = -kt \qquad \text{Eq. 4}$$

where k is the first order rate constant, C is the CH_3SH concentration after certain reaction time (t), and C_0 is the CH_3SH initial concentration. As shown in Table S1, the removal rate constant of 310-MnO_2 (0.00416 s^{-1}) is 1.4 times higher than that of 110-MnO_2 (0.00297 s^{-1}) and 1.74 times than that of 100-MnO_2 (0.00239 s^{-1}), which directly reveals the reaction rate at initial stage and also confirms the critical function of high index 310-facet again. Consistently, the turnover frequencies (TOFs, defined as the number of reactant molecules converted per active site in a unit of time) are also compared, which is in the rank of 310-MnO_2 (0.00246 h^{-1}) > 110-MnO_2 (0.00178 h^{-1}) >100-MnO_2 (0.00166 h^{-1}). The catalytic ozonation over MnO_2 usually proceeds via the Mars-van Krevelen mechanism. Generally, the surface oxygen species (O_{surf}) have greater mobility and activity than the lattice oxygen species (O_{latt}) and may give rise to beneficial spillover phenomena at the solid surface. Therefore, the availability and reactivity of O_{surf} play an important role in the activity of MnO_2. It is well known that O vacancies are directly related to active surface oxygen species. Thus, O vacancies act as active sites for catalytic ozonation.

Moreover, long-term catalytic stability of 310-MnO_2 was also investigated (Figure 4c), the removal efficiency of CH_3SH merely shows a subtle decline after 150 min, revealing a long-term stability of the catalyst, mainly due to the abundant oxygen vacancy in (310) facets. In contrast, (110) and (100) both displayed a significant decrease within 1 h. The slight deactivation for (310) MnO_2 is mainly due to the accumulation of the intermediate/product adsorbed on the oxygen vacancies can't be easily desorbed, evidenced by the great formation of new peaks belongs to sulfur and carbon species in the *In situ* DRIFTS (Fig. 6). To further explore whether the deactivation is reversible, the used catalysts were regenerated by ethanol/sulfuric acid and then utilized for following catalytic ozonation. As shown in Figure 4d, the removal efficiency of CH_3SH has improved a lot to almost approach the fresh state. Actually, ethanol could extract plugged species and H_2SO_4 could dissolve accumulated stuffs due to their polarity and acidity, respectively. [48-50]

3.5.2 ROS Generation in Catalytic Ozonation

Generally, the catalytic ozonation is strongly related to the transformation of decomposed ozone into atomic oxygen species (O^{2-}/O_2^{2-}) and further evolves into reactive oxygen species (ROSs) like as $^1O_2$, $\bullet O_2^-$, and $\bullet OH$, leading to their oxidative degradation and ultimate mineralization.[52, 53] First, *in situ* DRIFTS was conducted to identify the atomic oxygen species, a new peak belongs to oxygen species appears at 1380 cm^{-1} with O_3 purging to the 310-MnO_2, confirming the formation and accumulation of intermediate peroxide species (O^{2-}/O_2^{2-}) (Figure 5a).[28] Second, different chemical scavengers and ESR spectroscopy were collectively applied to identify the primary ROSs involved in the catalytic reaction of 310-MnO_2. As shown in Figure 5b, the CH_3SH removal efficiency of 310-MnO_2 was slightly declined to 88 % by adding tert-butanol (TBA, •OH scavenger), whereas that of 310-MnO_2 decreased dramatically to 68.1 % and 65.0 % in the presence of ascorbic acid (AA, $\bullet O_2^-$ scavenger) and NaN_3 ($^1O_2$ scavenger), revealing that both $\bullet O_2^-$ and $^1O_2$ exert dominating effect on CH_3SH degradation. Coincidently, the continuous generation of $\bullet O_2^-$ and $^1O_2$ by all the three MnO_2 was evidenced by the significant characteristic peaks of DMPO-$\bullet O_2^-$ (relative intensities of 1:1:1:1, Figure 5c) and TEMPO-$^1O_2$ (relative intensities of 1:1:1, Figure 5d).[51, 52] Although the characteristic spectrum of DMPO-•OH adducts was also observed, indicating •OH exerts a moderate effect in the present system (Figure 5e). Especially, the stronger signal of EPR peaks for 310-MnO_2 were achieved with respect to the other two samples, indicating the promoted active ROS generation caused by the engineered high-index (310) facets.

3.6 Conversion Pathway for CH_3SH Removal

To reveal the mechanism of adsorption and ozonation of CH_3SH over 310-MnO_2, *in-situ* DRIFTS was carried out to monitor time-related evolution of the reaction intermediates and final products on 310-MnO_2. As shown in Figure 6a, during adsorption process, a number of bands were appeared and greatly enhanced with time going at around 2965 cm^{-1} (stretch vibration of C-H), 976 cm^{-1} (S-C-H vibration), 840 cm^{-1} (C-H vibration), 1363 and 1423 cm^{-1} (δ_s-CH_3 and δ_{as}-CH_3), respectively, which are all derived from the adsorption and deformation of CH_3SH into CH_3S^- over catalyst. It suggested a portion of S-H bond were cleaved and CH_3SH was transformed into CH_3S^-, deriving from the chemisorption interaction between CH_3SH and Mn species.[46] Simultaneously, several new bands developed progressively can be designated as deprotonated sulfonic acid ($CH_3SO_3^-$) at 1192 cm^{-1} and the protonated acid (CH_3SO_3H) at 1153 cm^{-1}, indicating the adsorbed CH_3S^- was partially oxidized into $CH_3SO_3^-$. With prolonged adsorption time, COO^- stretch vibrating band (1656 and 1598 cm^{-1}), S-O stretching band (927 cm^{-1}), and sulfate band (SO_4^{2-}, 1036 cm^{-1}) appeared and increased, suggesting S-S and C-S bonds in $CH_3SO_3^-$ were broken and converted into SO_4^{2-} and COO^-. Actually, surface OH groups are greatly formed (3261 cm^{-1}) via water dissociation on oxygen vacancies or water-oxygen interactions on metal surfaces, which can be easily activated into ROS, thus take effects in the oxidation of CH_3SH during adsorption stage.[46]

The timely changes of *in-situ* DRIFTS for catalytic ozonation can be seen in Figure 6c. The baseline of adsorption equilibrium was the same as that of 20 min in Figure 6a. Obviously, the increasing peaks of OH/H_2O groups at 3261 cm^{-1} and 1620 cm^{-1} reveal the release of active OH species and the generation of H_2O during fierce oxidation. Correspondingly, many adsorption bands at 927, 976, 1423, 1363, 2965 and 2934 cm^{-1} corresponding to the adsorbed CH_3S^- species were significantly diminished and even disappeared, verifying the great consumption of chemisorbed CH_3S^- via oxidation. Interestingly, the peak related to $CH_3SO_3^-$ at 1215 cm^{-1} was increased in the initial 5 min and then sharply decreased in the following 20 min, suggesting $CH_3SO_3^-$ was the main intermediate product. With the further oxidation of $CH_3SO_3^-$, several new bands of C elements referring to $v_s(COO^-)$ at 1315 cm^{-1}, carbonate species (CO_3^{2-}) at 1421 cm^{-1} and Fermi doublet of CO_2 at 2334 and 2360 cm^{-1} were appeared and greatly boosted as the oxidation progressing, indicating that the cleaved C were utterly oxidized over the catalyst. In parallel, the bands of S products located at 1045 cm^{-1} (sulfate species, SO_4^{2-}) were also greatly intensified.

To clearly elucidate the tendency of product species evolution during these two stages, the normalized absorbance of intermediates and final products are illustrated in Figure 6b and 6d, which prove that the adsorption and transformation of CH_3SH are efficiently boosted on 310-MnO_2. As mentioned above, CH_3SH was greatly chemisorbed as CH_3S^- and partially oxidized by 310-MnO_2 during adsorption stage; after O_3 purged, the oxidation process was greatly enhanced, $CH_3SO_3^-$ was greatly formed as the intermediate product and subsequently decomposed into SO_4^{2-} and COO^-/CO_3^{2-} with CO_2 releasing afterwards. The results clearly confirm the efficient deep oxidation on mesoporous 310-MnO_2 with limited intermediate survived on the catalysts.

3.7 Surface Energies, Adsorption of Ozone and CH_3SH

To deepen the comprehension of the discrepancies in the affinity of exposed facets to O_3, the first-principles calculations are performed based on density functional theory using VASP program. As depicted in Figure 7a-c, the surface energies of three facets follow the order that 310 (1.57 J/m^2) > 110 (0.89 J/m^2) > 100 (0.96 J/m^2). Obviously, the highest surface energy of (310) facet signifies its best thermodynamic activity. According to Wulff construction theory, high energy facets have the tendency to vanish gradually in the bulk of crystals, thus to minimize the total surface energy of crystals and stabilize itself. Coincidently, (310) facets of α-MnO_2 can't be easily observed in most experiments, mainly due to its lower stability, higher surface energies and active sites. In the current case, due to the higher percentage of under-coordinated atoms and oxygen vacancies in high-index 310-MnO_2, the exposed high-energy facets thus can efficiently boost the efficiency of catalytic reactions, evidenced by its excellent performance in Figure 4b and 4c.

Generally, the reactions of catalytic ozonation are launched by the interactions between O_3 and the surface defects of catalysts, and its activity largely depends on the concentration and adsorption ability of the oxygen vacancy.[57] Firstly, XPS and Raman results above have identified (310) facets achieve higher concentration of oxygen vacancies on its surface, since (310) facets are readily to consume lower energy to form oxygen vacancies (E_{vo} (310) = 0.33 eV < E_{vo} (110) = 0.96 eV < E_{vo} (100) = 1.10 eV).[32] Secondly, since the strong adsorption of O_3 over the catalyst surface is favorable for the catalytic ozonation, the adsorption energy of O_3 over the oxygen vacancy of different facet MnO_2 was thus studied by DFT. As shown in Figure 7d-f, 310-MnO_2 facets exhibit the highest adsorption energy towards O_3 among the three-facet engineered

MnO_2: 310-MnO_2 (2.03 eV) > 110-MnO_2 (1.74 eV) > 100-MnO_2 (1.57 eV). The longer bond length of O-O (of adsorbed O_3, 1.24 Å) in 310-MnO_2 indicates that the bond of O_3 can be more easily broken and activated. Therefore, the strong adsorption of O_3 on 310-MnO_2 facet is beneficial for the formation of active oxygen species and the quick replenishment of surface active oxygen species, which is favorable for the catalytic ozonation of CH_3SH.

As the affinity and reactivity with O_3 and CH_3SH are both tightly related to the catalyst surface, the occurrence of competitive adsorption between O_3 and CH_3SH may inhibit the reaction. Therefore, the adsorption energy of CH_3SH over the oxygen vacancy of different facet MnO_2 was further studied by DFT. As shown in Figure 7g-h**,** CH_3SH molecule can be stablely adsorbed on 310-MnO_2 in a configuration with the adsorption energies of -1.69 eV kJ mol^{-1}, confirming the higher chemisorption of CH_3SH molecules induced by 310-MnO_2 than that of 100-MnO_2 and 110-MnO_2 (-1.25 and -1.41 kJ mol^{-1}), coincident well with the observed adsorption performance (Figure 4a). Notably, the adsorption energy of CH_3SH in 310-MnO_2 is -1.69 eV, which is higher than that of O_3 (-2.03 eV), indicating 310-MnO_2 possesses a more intact surface for O_3 than CH_3SH capture. Therefore, it can be proposed that 310-MnO_2 can firstly convert O_3 into reactive oxygen species and subsequently oxidize the neighbouring adsorbed CH_3SH. The step by step reaction ensure the sustainability of the entire process.

3.8 Mechanism of Adsorption and Catalytic Ozonation

Above performances and calculations have identified the great role of oxygen vacancy on the adsorption and catalytic ozonation for eliminating CH_3SH by 310-MnO_2. Therefore, a mechanism based on the involvement and circulation of oxygen vacancy is proposed, through probing changes of the chemical surface composition/state of the used 310-MnO_2 by XPS, XRD and *in situ* DRIFTS spectra. After adsorption stage, XPS results of O-1s and Mn-2p3/2 (Figure 2d, 2e and Table S2) show an evident increase in the ratio of O_{latt}/O_{ads} from 2.44 to 3.25, whereas a subtle decline in that of

Mn^{2+}+Mn^{3+}/Mn^{4+}, indicating the important role of O_{ads} rather than Mn to take effect on the oxidation of CH_3SH during adsorption stage. Actually, the consumed O_{ads} can be captured by oxygen vacancy and then transformed into active oxygen species, which play an important role in the partial oxidation of chemisorbed CH_3S^-.[46, 57]

After catalytic ozonation, the molar ratio of Mn^{2+}+Mn^{3+}/Mn^{4+} significantly decreased from 1.11 to 0.84 and the surface average oxidation state (AOS) of Mn decreased from 0.528 to 0.515 (Figure 2d, 2f and Table S2), indicating that the oxygen vacancies of 310-MnO_2 decreased after catalytic ozonation. Generally, when O_3 flows through MnO_2, O_3 molecule binds to MnO_2 surface by inserting an O atom into an oxygen vacancy site.[1, 6] The oxygen vacancy is a 2-electron donor and transfer 2-electron to an O atom of O_3, thus forming an activate oxygen species (O^{2-}) in the oxygen vacancy site and an oxygen molecule, which desorbs into the air (Eq. 5).[8, 9] Then another O_3 molecule reacts with O^{2-} to produce a gas-phase oxygen molecule and a bridging O_2 dimer (peroxide, O_2^{2-}) species (Eq. 6). *In situ* DRIFTS in Figure 4d confirms the formation of peroxide species (O^{2-}/O_2^{2-}). Further, the reaction between O^{2-}/O_2^{2-}-active species and ozone molecules occurred along with the evolution of oxygen molecules ($\cdot O_2^-$/$^1O_2$/$\cdot OH$) via charge-transfer interactions. During the above-mentioned reactions, the oxygen-related intermediates gradually accumulated on 310-MnO_2 surfaces and simultaneously transformed into oxygen molecules to release a portion of oxygen vacancies to maintain the electrostatic balance.[53] Therefore, due to more oxygen vacancy and un-coordinated Mn-Mn bond in the MnO_6 octahedral chains of 310-MnO_2, it can promote the decomposition speed of O_3 and likely produce more active oxygen species in the local area of the catalyst.

In conclusion, the proposed reaction pathway for catalytic ozonation of CH_3SH over 310-MnO_2 was established in Figure 8.[9, 53] O_3 can be captured and decomposed by the structural defects (Vo, mostly the oxygen vacancies) on MnO_2 surface; then transformed into activate oxygen species (O^{2-}/O_2^{2-}) and quickly evolved into $\cdot O_2^-$/$\cdot OH$/$^1O_2$ through a chain cycle reaction, which can directly participate in CH_3SH and adsorbed CH_3S^- oxidation (Eq. 7-9). And these defects can be regenerated through the cycle thus to maintain a long-term removal efficiency (Eq. 7). Hence, the presence of more surface oxygen vacancies was beneficial to the highly efficient catalytic ozonation on 310-MnO_2. Given the importance of oxygen vacancy in the catalytic ozonation, engineering the crystalline structure of MnO_2 with abundant oxygen vacancy will provide promising perspectives in purification of odor gas.

$$O_3 + Vo \rightarrow O_2 + O^{2-} \qquad \text{Eq. 5}$$

$$O^{2-} + O_3 \rightarrow O_2 + O_2^{2-} \qquad \text{Eq. 6}$$

$$O_2^{2-} \rightarrow O_2 + Vo \qquad \text{Eq. 7}$$

$$O^{2-}/O_2^{2-} + H_2O \rightarrow \cdot O_2^-/^1O_2/\cdot OH \qquad \text{Eq. 8}$$

$$CH_3SH/CH_3S^- + \cdot O_2^-/^1O_2/\cdot OH \rightarrow CH_3SO_3^- \rightarrow SO_4^{2-} + CO_3^{2-}/CO_2 \qquad \text{Eq. 9}$$

Environmental implication

In this study, facet engineered MnO_2 was prepared and efficiently utilized for catalytic ozonation of CH_3SH. In addition, a combination of both experimental and DFT calculation results confirmed the key role of oxygen vacancies in the catalytic reaction process, evidenced by the positive correlation between oxygen vacancy and activity. To promote the applicability of 310-MnO_2 in view of practice , mesoporous Al_2O_3 supports were used to immobilize α-MnO_2, as it can provide the extensive reactive sites for enhancing retention time and practicability for reuse.[26] Compared with the bare Al_2O_3, the immobilized MnO_2 leads to a decline in the surface area/pore size (238.2 m^2g^{-1}/4.1 nm) of 310-MnO_2/Al_2O_3 and clearly observed XRD patterns of 310-MnO_2 (Figure S2-S3, Table S3-S4), confirming the 310-MnO_2 are well deposited on the surface and into the channels of Al_2O_3.[33] As depicted in Figure S4, within 800 s reaction, 310-MnO_2/Al_2O_3 can realize 100% removal efficiency for 70 ppm of CH_3SH, faster than that of 310-MnO_2 alone. These results provided a new perspective for catalysts applied for catalytic ozonation. This work has a proper strategy recommendation for translating laboratory research into commercial value to eliminate odor gas via the efficient and cost-effective catalytic oxidation to attain the standard protocols of air quality.

Acknowledgments

The authors wish to thank the National Natural Science Foundation of China (No. 51578556, 21876212, 41573086, 41603097, 21976214), Natural Science Foundation of Guangdong Province (No. 2015A030308005 , S2013010012927, S2011010003416), Science and Technology Research Programs of Guangdong Province (No. 2014A020216009, 2019A1515011015), the Science and Technology Program of Guangzhou (201904010353), and Fundamental Research Funds for the Central Universities (13lgjc10, 19lgpy157) for financially supporting this work. Dr. Xia was also supported by the Start-up Funds for High-Level Talents of Sun Yat-sen University (38000-18821111).

Appendix A. supplementary data associated with this article can be found. H_2-TPR, Raman and degradation rate constant of three facet MnO_2 (Table S1), XPS analysis of 310-MnO_2 before and after catalytic ozonation (Table S2), EDS analysis of 310-MnO_2/Al_2O_3 (Table S3), BET analysis of 310-MnO_2/Al_2O_3 (Table S4), schematic diagram of setup (Figure S1), N_2 adsorption-desorption isotherm and pore-size distribution of 310-MnO_2/Al_2O_3 (Figure S2), XRD, SEM, EDS spectra and elemental mapping of 310-MnO_2/Al_2O_3 (Figure S3), Performances in catalytic ozonation of CH_3SH with 310-MnO_2/Al_2O_3 (Figure S4).

References

1. Huang, J.; Zhong, S.; Dai, Y.; Liu, C. C.; Zhang, H. Effect of MnO_2 phase structure on the oxidative reactivity toward Bisphenol A degradation. *Environ. Sci. Technol.* **2018,** *52*, 11309-11318.

2. Lu, J.; Hao, H.; Zhang, L.; Xu, Z.; Zhong, L.; Zhao, Y.; He, D.; Liu, J.; Chen, D.; Pu, H.; He, S.; Luo, Y. The investigation of the role of basic lanthanum (La) species on

the improvement of catalytic activity and stability of HZSM-5 material for eliminating methanethiol (CH_3SH). *Appl. Catal., B* **2018,** *237*, 185-197.

3. Kastner, J. R.; Das, K. C.; Buquoi, Q.; Melear, N. D. Low temperature catalytic oxidation of hydrogen sulfide and methanethiol using wood and coal fly ash. *Environ. Sci. Technol.* **2003,** *37*, 2568-2574.

4. Omri, I.; Bouallagui, H.; Aouidi, F.; Godon, J.-J.; Hamdi, M. H_2S gas biological removal efficiency and bacterial community diversity in biofilter treating wastewater odor. *Bioresour. Technol.* **2011,** *102*, 10202-10209.

5. Bashkova, S.; Bagreev, A.; Bandosz, T. J. Adsorption of methyl mercaptan on activated carbons. *Environ Sci Technol* **2002,** *36*, 2777-2782.

6. Roman, P.; Veltman, R.; Bijmans, M. F. M.; Keesman, K. J.; Janssen, A. J. H. Effect of methanethiol concentration on sulfur production in biological desulfurization systems under haloalkaline conditions. *Environ. Sci. Technol.* **2015,** *49*, 9212-9221.

7. Estrada, J. M.; Kraakman, N. J. R. B.; Munoz, R.; Lebrero, R. A comparative analysis of odour treatment technologies in wastewater treatment plants. *Environ. Sci. Technol.* **2011,** *45*, 1100-1106.

8. He, D.; Wan, G.; Hao, H.; Chen, D.; Lu, J.; Zhang, L.; Liu, F.; Zhong, L.; He, S.; Luo, Y. Microwave-assisted rapid synthesis of CeO_2 nanoparticles and its desulfurization processes for CH_3SH catalytic decomposition. *Chem. Eng. J.* **2016,** *289*, 161-169.

9. Wang, H.; Huang, Z.; Jiang, Z.; Jiang, Z.; Zhang, Y.; Zhang, Z.; Shangguan, W. Trifunctional C@MnO catalyst for enhanced stable simultaneously catalytic removal of formaldehyde and ozone. *ACS Catal.* **2018,** *8*, 3164-3180.

10. Rezaei, E.; Soltan, J.; Chen, N.; Lin, J. Effect of noble metals on activity of MnOx/γ-alumina catalyst in catalytic ozonation of toluene. *Chem. Eng. J.* **2013,** *214*, 219-228.

11. Jia, J.; Zhang, P.; Chen, L. Catalytic decomposition of gaseous ozone over manganese dioxides with different crystal structures. *Appl. Catal., B* **2016,** *189*, 210-218.

12. Zhang, J.; Li, Y.; Wang, L.; Zhang, C.; He, H. Catalytic oxidation of formaldehyde over manganese oxides with different crystal structures. *Catal. Sci. Technol.* **2015,** *5*, 2305-2313.

13. Wang, F.; Dai, H.; Deng, J.; Bai, G.; Ji, K.; Liu, Y. Manganese oxides with rod-, wire-, tube-, and flower-like morphologies: highly effective catalysts for the removal of toluene. *Environ Sci Technol* **2012,** *46*, 4034-4041.

14. Xie, X.; Li, Y.; Liu, Z.-Q.; Haruta, M.; Shen, W. Low-temperature oxidation of CO catalysed by Co_3O_4 nanorods. *Nature* **2009,** *458*, 746-749.

15. Zhang, B.; Wang, D.; Hou, Y.; Yang, S.; Yang, X. H.; Zhong, J. H.; Liu, J.; Wang, H. F.; Hu, P.; Zhao, H. J.; Yang, H. G. Facet-dependent catalytic activity of platinum nanocrystals for triiodide reduction in dye-sensitized solar cells. *Sci. Rep.* **2013,** *3, 1836.*

16. Tian, N.; Zhou, Z.-Y.; Sun, S.-G.; Ding, Y.; Wang, Z. L. Synthesis of tetrahexahedral platinum nanocrystals with high-index facets and high electro-oxidation activity. *Science* **2007,** *316*, 732-735.

17. Yang, H. G.; Sun, C. H.; Qiao, S. Z.; Zou, J.; Liu, G.; Smith, S. C.; Cheng, H. M.; Lu, G. Q. Anatase TiO_2 single crystals with a large percentage of reactive facets. *Nature* **2008,** *453*, 638-U4.

18. Penn, R. L.; Banfield, J. F. Morphology development and crystal growth in nanocrystalline aggregates under hydrothermal conditions: Insights from titania. *Geochim. Cosmochim. Acta* **1999,** *63*, 1549-1557.

19. Dinh, C.-T.; Nguyen, T.-D.; Kleitz, F.; Do, T.-O. Shape-controlled synthesis of highly crystalline titania nanocrystals. *ACS Nano* **2009,** *3*, 3737-3743.

20. Li, W.; Gibbs, G. V.; Oyama, S. T. Mechanism of ozone decomposition on a manganese oxide catalyst. 1. In situ ramanspectroscopy and Ab Initio molecular orbital calculations. *J. Am. Chem. Soc.* **1998**, 120 (35), 9041-9046.

21. Einaga, H.; Maeda, N.; Yamamoto, S.; Teraoka, Y. Catalytic properties of copper-manganese mixed oxides supported on SiO_2 for benzene oxidation with ozone. *Catal. Today* **2015,** *245*, 22-27.

22. Einaga, H.; Teraoka, Y.; Ogat, A. Benzene oxidation with ozone over manganese oxide supported on zeolite catalysts. *Catal. Today* **2011,** *164*, 571-574.

23. Einaga, H.; Teraoka, Y.; Ogata, A. Catalytic oxidation of benzene by ozone over manganese oxides supported on USY zeolite. *J. Catal.* **2013,** *305*, 227-237.

24. Rezaei, E.; Soltan, J.; Chen, N. Catalytic oxidation of toluene by ozone over alumina supported manganese oxides: effect of catalyst loading. *Appl. Catal., B* **2013,** *136*, 239-247.

25. Ma, J.; Sui, M. H.; Chen, Z. L.; Wang, L. N. Degradation of refractory organic pollutants by catalytic ozonation-activated carbon and Mn-loaded activated carbon as catalysts. *Ozone: Sci. Eng.* **2004,** *26*, 3-10.

26. Bing, J.; Hu, C.; Zhang, L. Enhanced mineralization of pharmaceuticals by surface oxidation over mesoporous γ-Ti-Al_2O_3 suspension with ozone. *Appl. Catal., B* **2017,** *202*, 118-126.

27. Kresse; Furthmuller. Efficient iterative schemes for ab initio total-energy calculations using a plane-wave basis set. *Phys. Rev. B: Condens. Matter Mater. Phys.* **1996,** *54*, 11169-11186.

28. Kresse, G.; Joubert, D. From ultrasoft pseudopotentials to the projector augmented-wave method. *Phys. Rev. B* **1999,** *59*, 1758-1775.

29. Perdew, J. P.; Burke, K.; Ernzerhof, M. Generalized gradient approximation made simple. *Phys. Rev. Lett.* **1996,** *77*, 3865-3868.

30. Crespo, Y.; Seriani, N. Electronic and magnetic properties of alpha-MnO_2 from ab initio calculations. *Phys. Rev. B* **2013,** *88,* 144428.

31. Tompsett, D. A.; Parker, S. C.; Bruce, P. G.; Islam, M. S. Nanostructuring of beta-MnO_2: The Important Role of Surface to Bulk Ion Migration. *Chem. Mater.* **2013,** *25*, 536-541.

32. Rong, S.; Zhang, P.; Liu, F.; Yang, Y. Engineering crystal facet of α-MnO_2 nanowire for highly efficient catalytic oxidation of carcinogenic airborne formaldehyde. *ACS Catal.* **2018,** *8*, 3435-3446.

33. Xia, D.; Hu, L.; Tan, X.; He, C.; Pan, W.; Yang, T.; Huang, Y.; Shu, D. Immobilization of self-stabilized plasmonic Ag-AgI on mesoporous Al_2O_3 for efficient purification of industrial waste gas with indoor LED illumination. *Appl. Catal., B* **2016,** *185*, 295-306.

34. Mathew, T.; Suzuki, K.; Ikuta, Y.; Takahashi, N.; Shinjoh, H. Mesoporous ferrihydrite with incorporated manganese for rapid removal of organic contaminants in air. *Chem. Commun.* **2012,** *48*, 10987-10989.

35. Wang, J.; Li, D.; Li, P.; Zhang, P.; Xu, Q.; Yu, J. Layered manganese oxides for formaldehyde-oxidation at room temperature: the effect of interlayer cations. *Rsc Advances* **2015,** *5*, 100434-100442.

36. Yang, R.; Ren, C.; Teng, X.; Chen, Z.; Wu, S.; Zhang, W. Study of the surface oxygen vacancies evolvement on the single and Bi-components manganese oxide precursors and their catalytic performance. *Catal. Lett.* **2017,** *147*, 727-737.

37. Feng, Z.; Huang, L.; Feng, Q.; Li, X.; Zhang, H.; Tang, W.; Zhang, J.; Hao, Y. Influence of annealing atmosphere on the performance of a beta-Ga_2O_3 thin film and photodetector. *Opt. Mater. Express* **2018,** *8*, 2229-2237.

38. Polverejan, M.; Viliegas, J. C.; Suib, S. L. Higher valency ion substitution into the manganese oxide framework. *J. Am. Chem. Soc.* **2004,** *126*, 7774-7775.

39. Piumetti, M.; Fino, D.; Russo, N. Mesoporous manganese oxides prepared by solution combustion synthesis as catalysts for the total oxidation of VOCs. *Appl. Catal., B* **2015,** *163*, 277-287.

40. Qu, Z.; Bu, Y.; Qin, Y.; Wang, Y.; Fu, Q. The improved reactivity of manganese catalysts by Ag in catalytic oxidation of toluene. *Appl. Catal., B* **2013,** *132*, 353-362.

41. Wei, Y. J.; Yan, L. Y.; Wang, C. Z.; Xu, X. G.; Wu, F.; Chen, G. Effects of Ni doping on MnO_6 octahedron in $LiMn_2O_4$. *J. Phys. Chem. B* **2004,** *108*, 18547-18551.

42. Selloni, A. Crystal growth - Anatase shows its reactive side. *Nat.Mater.* **2008,** *7*, 613-615.

43. Vittadini, A.; Selloni, A.; Rotzinger, F. P.; Gratzel, M. Structure and energetics of water adsorbed at TiO_2 anatase (101) and (001) surfaces. *Phys. Rev. Lett.* **1998,** *81*, 2954-2957.

44. Van Santen, R. A. Complementary structure sensitive and insensitive catalytic relationships. *Acc. Chem. Res.* **2009,** *42*, 57-66.

45. Li, Y.; Fan, Z.; Shi, J.; Liu, Z.; Shangguan, W. Post plasma-catalysis for VOCs degradation over different phase structure MnO_2 catalysts. *Chem. Eng. J.* **2014,** *241*, 251-258.

46. Xia, D.; Xu, W.; Wang, Y.; Yang, J.; Huang, Y.; Hu, L.; He, C.; Shu, D.; Leung, D. Y. C.; Pang, Z. Enhanced performance and conversion pathway for catalytic ozonation of methyl mercaptan on single-Atom Ag deposited three-dimensional ordered mesoporous MnO_2. *Environ. Sci. Technol.* **2018,** *52*, 13399-13409.

47. Liu, C. S.; Zhang, L. J.; Feng, C. H.; Wu, C. A.; Li, F. B.; Li, X. Z. Relationship between oxidative degradation of 2-mercaptobenzothiazole and physicochemical properties of manganese (hydro)oxides. *Environ. Chem.* **2009,** *6*, 83-92.

48. Su, G.; Li, Q.; Lu, H.; Zhang, L.; Huang, L.; Yan, L.; Zheng, M. Thermal catalytic oxidation of octachloronaphthalene over anatase TiO_2 nanomaterial and its hypothesized mechanism. *Sci. Rep.* **2015,** *5*, 1-11.

49. Afzal, S.; Quan, X.; Zhang, J. High surface area mesoporous nanocast $LaMO_3$ (M = Mn, Fe) perovskites for efficient catalytic ozonation and an insight into probable catalytic mechanism. *Appl. Catal., B* **2017,** *206*, 692-703.

50. Lai, T.-L.; Lai, Y.-L.; Lee, C.-C.; Shu, Y.-Y.; Wang, C.-B. Microwave-assisted rapid fabrication of Co_3O_4 nanorods and application to the degradation of phenol. *Catal. Today* **2008,** *131*, 105-110.

51. Ozawa, T.; Miura, Y.; Ueda, J.-I. Oxidation of spin-traps by chlorine dioxide (ClO^{-2}) radical in aqueous solutions: First ESR evidence of formation of new nitroxide radicals. *Free Radicals Biol. Med.* **1996,** *20*, 837-841.

52. Ueda, J.; Takeshita, K.; Matsumoto, S.; Yazaki, K.; Kawaguchi, M.; Ozawa, T. Singlet oxygen-mediated hydroxyl radical production in the presence of phenols: Whether DMPO-(OH)-O-center dot formation really indicates production of (OH)-O-center dot? *Photochem. Photobiol.* **2003,** *77*, 165-170.

53. Long, L.; Zhao, J.; Yang, L.; Fu, M.; Wu, J.; Huang, B.; Ye, D. Room Temperature Catalytic Ozonation of Toluene over MnO_2/Al_2O_3. *Chin. J. Catal.* **2011,** *32*, 904-916.

54. Zhu G.; Zhu J.; Li L.; Yao W.; Zong R.; Zhu Y.; Zhang Q. Tuning the K^+ Concentration in the Tunnels of α-MnO_2 To Increase the Content of Oxygen Vacancy for Ozone Elimination. *Environ Sci Technol.* **2018,** 52, 8684-8692.

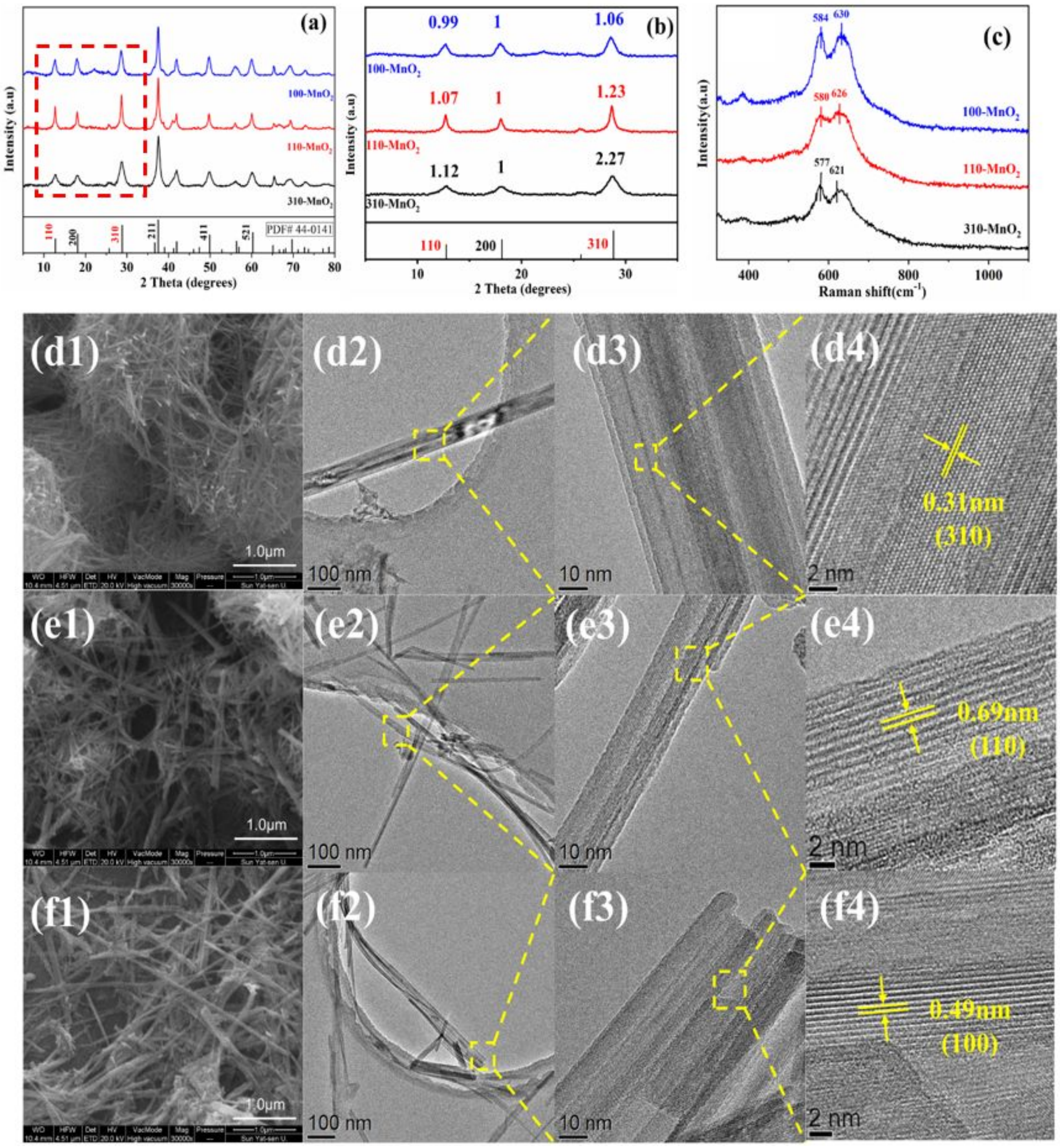

Figure 1. (a) XRD pattern, (b) magnified XRD patterns with a relative intensity comparison of different peaks, all the intensity of (200) peak were set as normalized one) and (c) Raman spectra of pure α-MnO$_2$ with different exposed facets; SEM images of (d1) 310-MnO$_2$; (e1) 110-MnO$_2$; (f1) 100-MnO$_2$, and TEM and HRTEM images of

(d2-d4) 310-MnO_2; (e2-e4) 110-MnO_2; (f2-f4) 100-MnO_2.

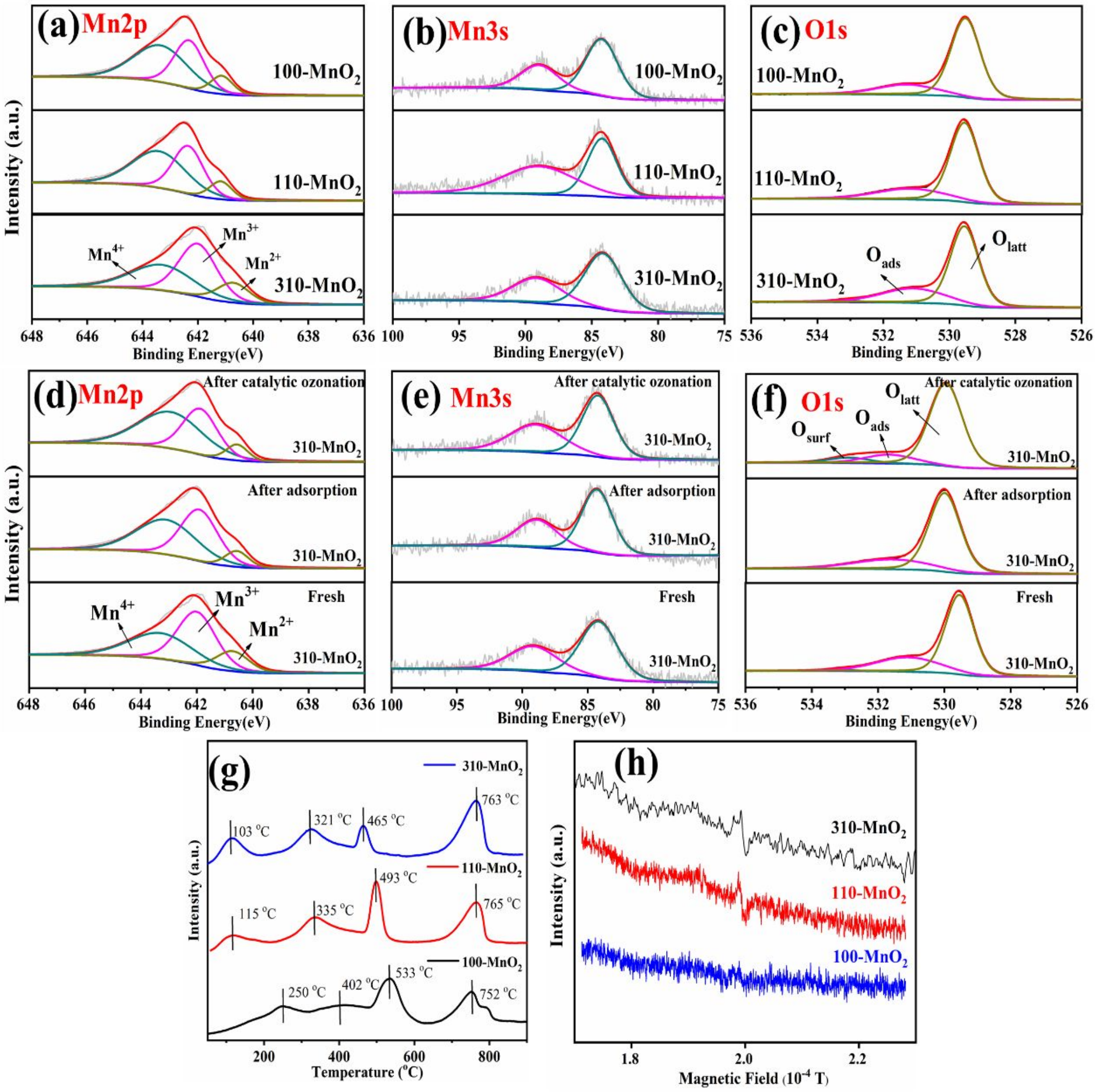

Figure 2. XPS spectra of Mn 2p (a, d), Mn 3s (b, e) and O 1s (c, f) for fresh different MnO_2 (upper row); different MnO_2 after deep adsorption of CH_3SH, different MnO_2 after deep catalytic ozonation of CH_3SH (lower row); (g) O_2-TPD profiles of facet engineered MnO_2 (h) EPR profiles.

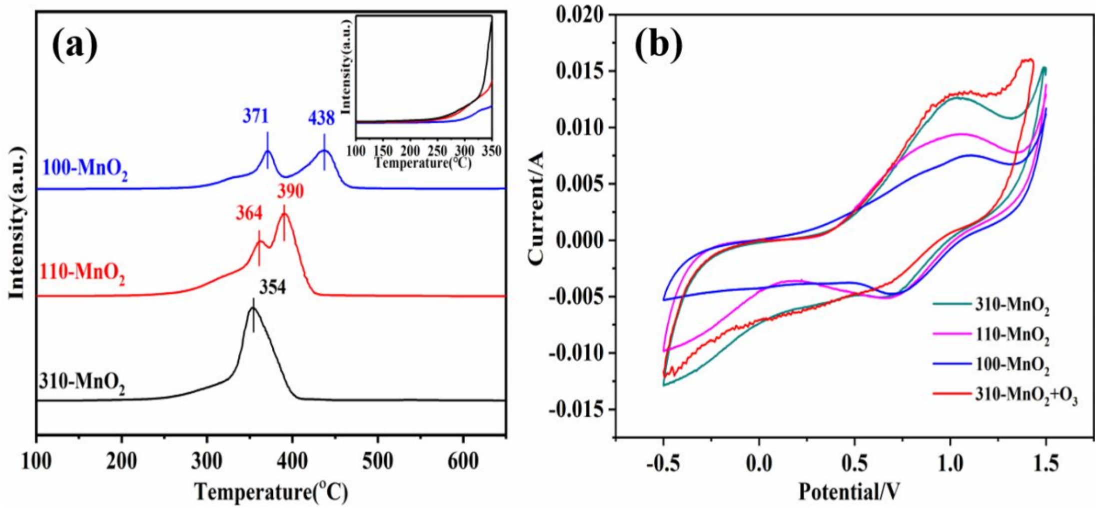

Figure 3. (a) H_2-TPR profiles; (b) CV curves with different exposed MnO_2 facets.

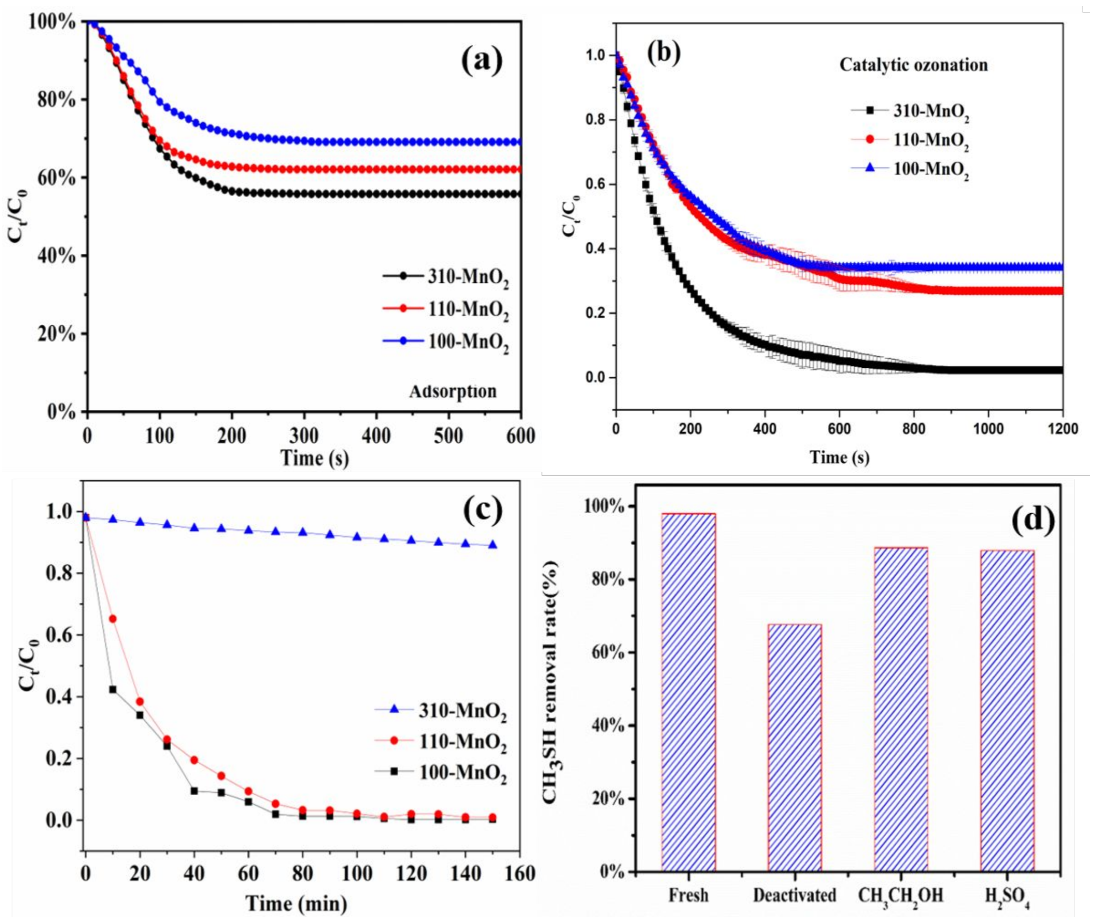

Figure 4. Performances in adsorption (a) and catalytic ozonation (b) of CH_3SH in different MnO_2, (c) Removal of CH_3SH in long-term runs using facet engineered MnO_2, (d) Catalytic ozonation removal rate of CH_3SH by regenerated 310-MnO_2 with ethanol and sulfuric acid.

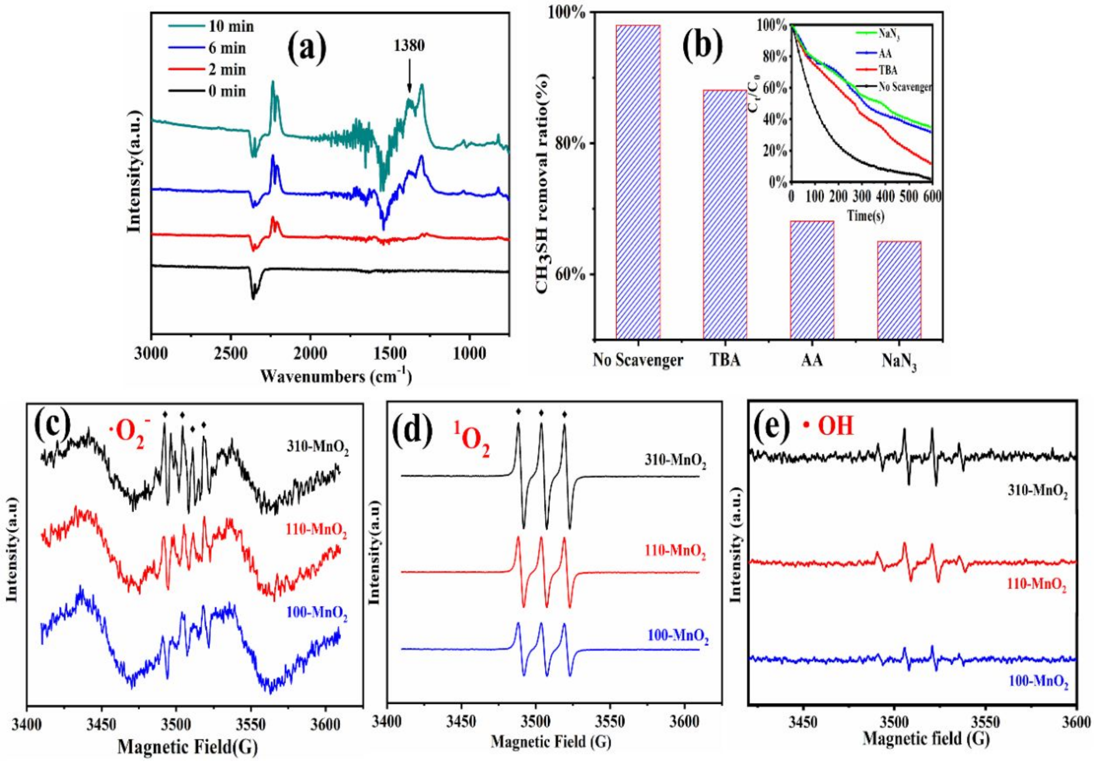

Figure 5. (a) *In situ* DRIFTS spectra of the 310-MnO$_2$ with O$_3$ purging to detect atomic oxygen; (b) Catalytic ozonation of CH$_3$SH by 310-MnO$_2$ with different scavengers; ESR signals of (c) •O$_2^-$, (d) ^{1}O$_2$ and (e) •OH.

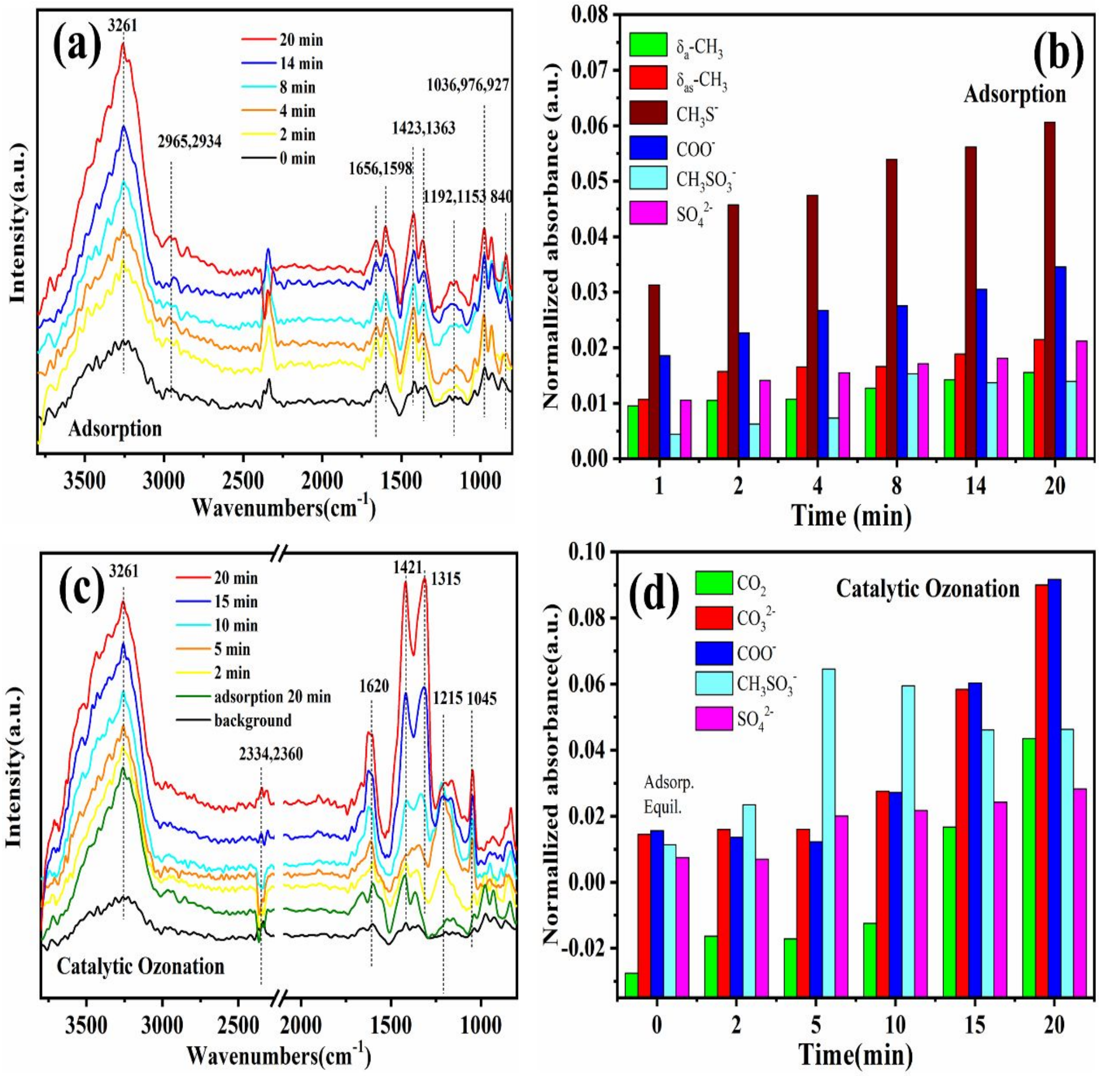

Figure 6. *In-situ* DRIFTS spectra of (a) adsorption, (c) catalytic ozonation for CH_3SH with 310-MnO_2; normalized species evolution of (b) adsorption, (d) catalytic ozonation for CH_3SH with 310-MnO_2.

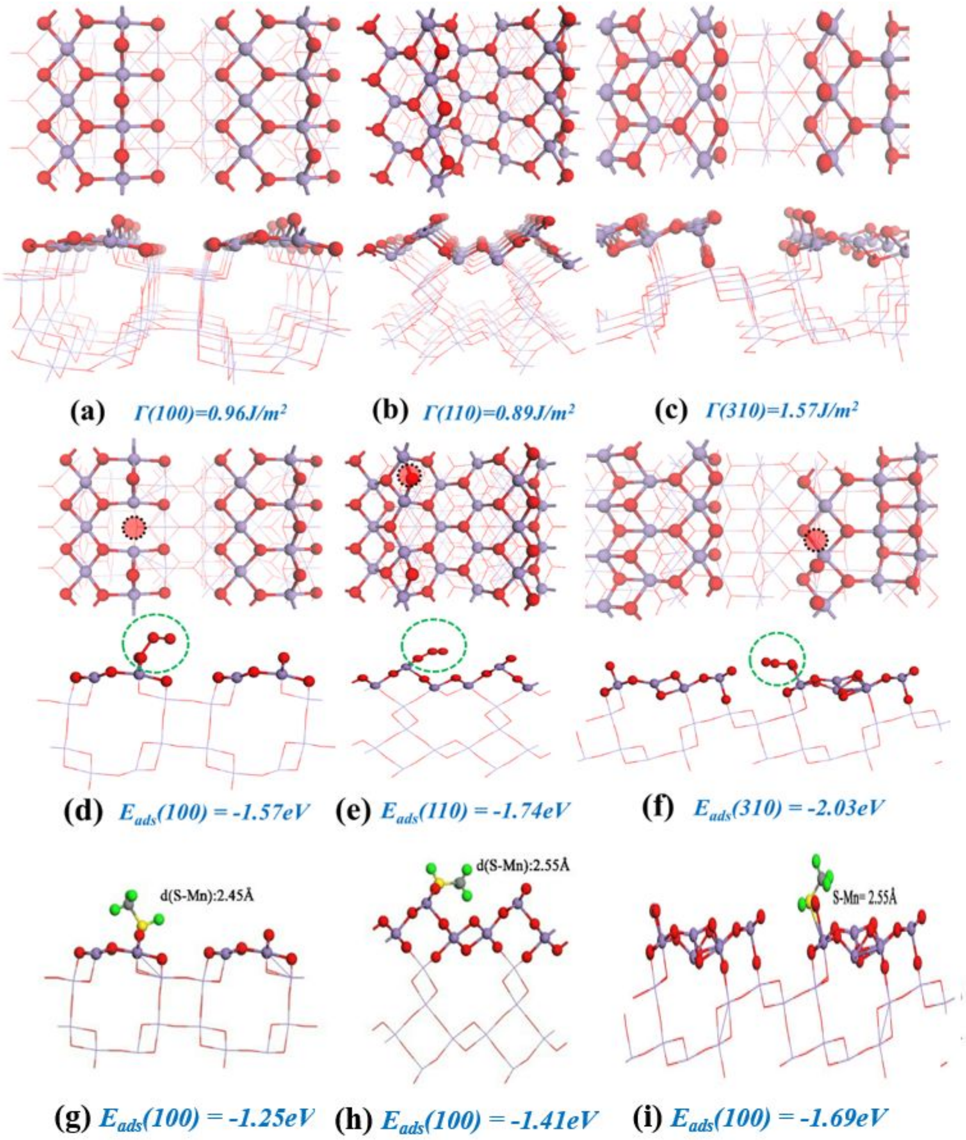

Figure 7. (a-c) Surface energy of *α*-MnO_2 with different exposed facets; (d-f) adsorption energy of O_3 on oxygen vacancy of α-MnO_2 with different exposed facets; (g-i) adsorption energy of S atom in CH_3SH on oxygen vacancy of α-MnO_2 with different exposed facets. Red sphere stands for oxygen atom and violet sphere stands for manganese atom.

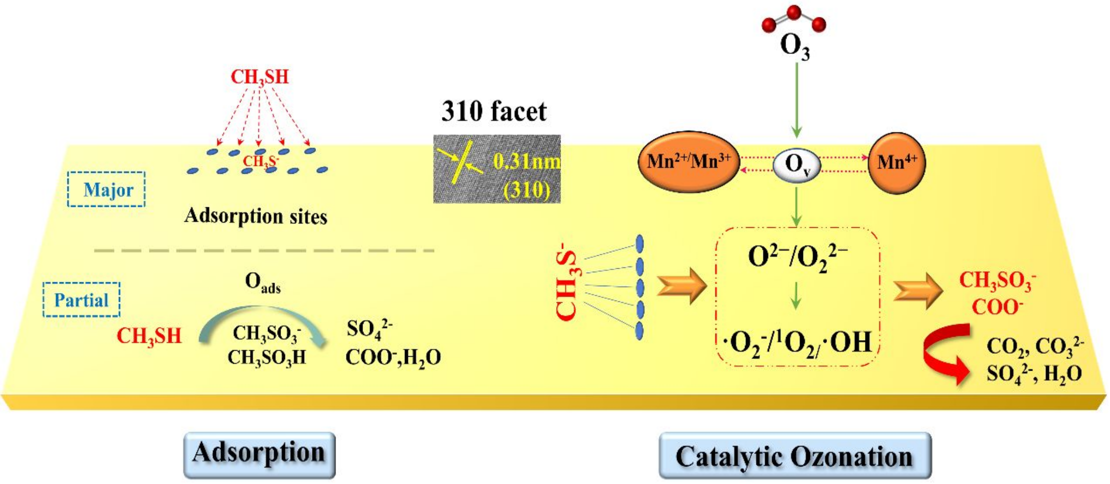

Figure 8. Mechanism of adsorption and catalytic ozonation toward CH_3SH by 310-α-MnO_2 catalysts.

Graphical Abstract